A polarizing Fourier transform spectrometer for astronomical spectroscopy at submillimeter and mid-infrared wavelengths

David A. Naylor

Department of Physics, University of Lethbridge
Lethbridge, Alberta T1K 3M4, Canada

T. Alan Clark

Department of Physics and Astronomy, University of Calgary
Calgary, Alberta T2N 1N4, Canada

Gary R. Davis

Institute of Space and Atmospheric Studies, University of Saskatchewan
Saskatoon, Saskatchewan S7N 0W0, Canada

ABSTRACT

The design of a polarizing Fourier transform spectrometer, developed for submillimeter and mid-infrared astronomical spectroscopy, is presented. Results from recent observing runs are used to illustrate its performance.

1 INTRODUCTION

Astronomical spectroscopy at submillimeter and infrared wavelengths holds much promise for fields as diverse as the study of solar and planetary atmospheres, molecular clouds and extragalactic sources. To varying degrees, ground based observations over this spectral range are made difficult by the partial and variable transmission of the atmospheric windows, with submillimeter and mid-infrared observations being the most difficult. At submillimeter wavelengths, Fourier transform spectrometers afford the only practical solution to broad-band, intermediate resolution, astronomical spectroscopy. While Fourier spectrometers have intrinsically lower spectral resolution than heterodyne receivers, they are ideally suited to applications which require broad spectral coverage. Potential areas of study include: pressure broadened absorption lines of constituents in planetary atmospheres, the search for, and identification of, spectral features in the atmospheres of the sun and planets and in molecular clouds, broad line emission from extragalactic sources and measurements of dust continuum emission.

In this paper we present the design of a polarizing Fourier transform spectrometer (FTS) which has been developed for astronomical spectroscopy at submillimeter and mid-infrared wavelengths. The spectrometer has been used at the James Clerk Maxwell Telescope (JCMT) in a program of planetary and solar submillimeter spectroscopy. More recently, the spectrometer was operated at the NASA Infrared Telescope Facility (IRTF) where it was used, in conjunction with a small heliostat, to measure the solar spectrum at 20μm, both as a scientific objective in itself, and as a method of assessing its merit as a mid-infrared astronomical spectrometer. These represented the first astronomical observations to be conducted with a polarizing FTS at a wavelength of 20μm and resulted in the detection of the hydrogen n = 8–7 recombination line in emission and several OH lines in absorption in the solar spectrum. Results from both these programs will be presented to illustrate the performance of the spectrometer.

2 POLARIZING FOURIER TRANSFORM SPECTROMETER

2.1 Background

In February 1990, an existing classical infrared Michelson interferometer[1], modified to operate at submillimeter wavelengths, was used to measure the atmospheric transmission above Mauna Kea. The goal of these measurements was to determine the feasibility of conducting intermediate resolution, broad-band astronomical spectroscopic observations from the JCMT[2]. The atmospheric transmission spectra obtained during this observing run were found to be in close agreement with theoretical atmospheric models. The experience gained with that interferometer led to the development of the polarizing FTS described in this paper. The design is based on the two-beam Martin-Puplett interferometer[3] and offers several advantages over a classical Michelson interferometer which are of particular importance in astronomical spectroscopy.

0-8194-1493-X/94/$6.00

First, the modulation efficiency of a metal grid beamsplitter is both high and uniform over a wide spectral range. For a grid spacing d this spectral range extends from 0 to $\sim \frac{1}{4d}$ cm^{-1}. Thus the reflection and transmission coefficients for a 10μm period grid are close to 100% for the appropriate planes of polarization over the range 0 to 250 cm^{-1}. In contrast, the modulation efficiency of a classical dielectric beamsplitter exhibits a characteristic lobe pattern with only moderate efficiency at the bandcenter, and much lower efficiency at other wavelengths. In principle, the polarizing interferometer can operate out to the above wavelength limit but in practice, the spectral bandpass is determined by filters in the detector subsystem which are matched to the available atmospheric windows. This makes for efficient use of limited observing time, for in the event that transmission in the submillimeter windows becomes poor, the FTS can be reconfigured in a matter of seconds to operate in the higher transmission millimeter windows simply by changing the filter in the detector subsystem.

Second, in comparison to a Michelson interferometer which has only one input and one output port, a polarizing interferometer provides two input and two output ports. In a balanced system, a detector at either of the output ports records the difference between radiation entering the two input ports. This differential measurement is necessary when one is trying to detect a weak astronomical signal in the presence of a large atmospheric emission component. In a typical astronomical observation the second port views a background sky position which is offset from the source position, but at the same airmass, and thus provides effective cancellation of atmospheric emission (but not transmission) variations. This cancellation is essential at submillimeter wavelengths where sky emission fluctuation is the dominant source of noise. Since the interferometric signals at the two output ports are complementary, signals obtained from matched detectors, placed at each port, can be subtracted to double the modulated component of the interferogram while essentially eliminating any unmodulated component. (The two output ports can also be exploited to observe simultaneously in two different wavelength ranges, eg. at 10 and 20μm.)

Third, since radiation polarization is encoded by the input polarizer and decoded by the output analyser, only radiation passing through both polarizers can be detected interferometrically, simplifying calibration of the resulting spectra. By comparison, in a Michelson interferometer, the detector can *see* its own environment (the so called *anti-interferogram*, the $R^2 + T^2$ term.) which may vary with time and this can lead to significant uncertainties in calibration.

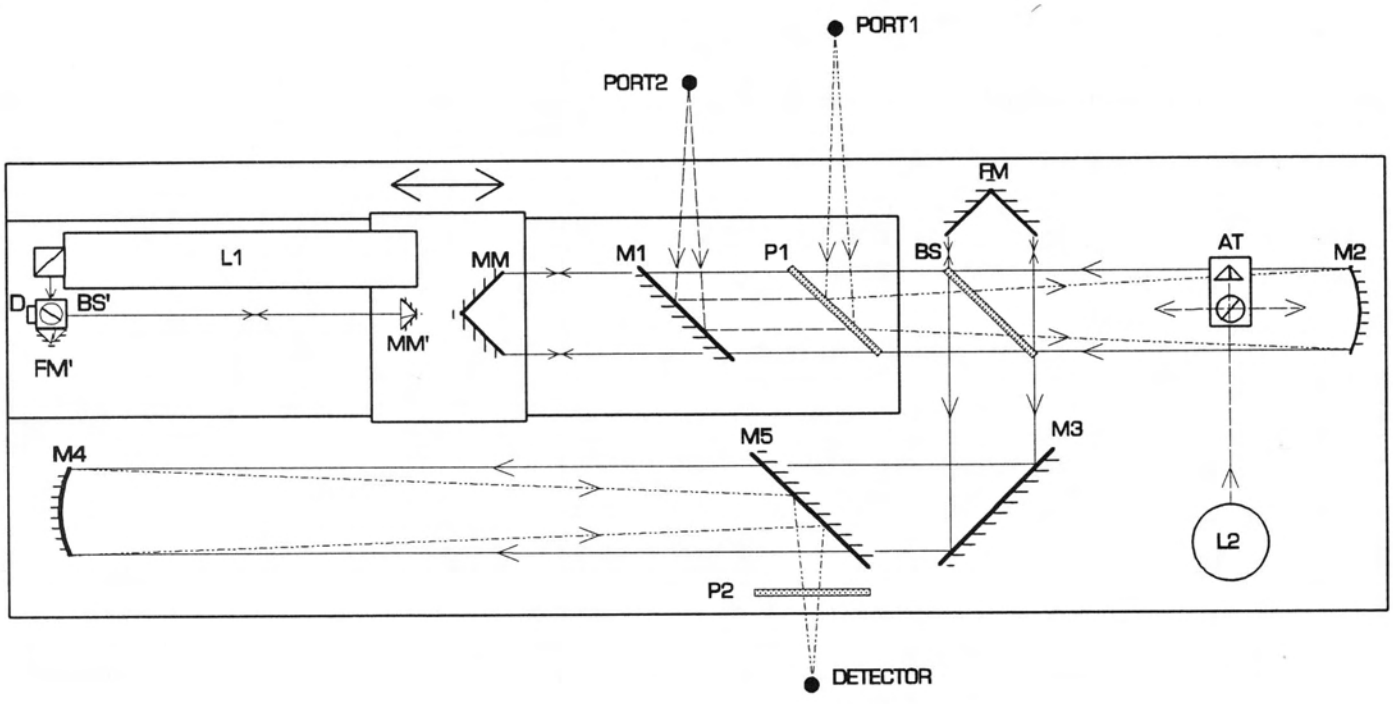

Fig. 1 Schematic of polarizing Fourier transform spectrometer optics

2.2 Optical design

The polarizing FTS is designed to mount at the east Nasmyth f/35 focus of the JCMT, between the elevation bearing of the telescope and the bolometric facility detector, UKT14. The optical layout of the interferometer is shown in fig. 1 and its characteristics are listed in Table 1.

The interferometer is mounted upon a damped optical breadboard, with optical components housed in high-precision adjustable mounts on two levels. Components M1, P1, M5, P2 are on the upper level, while the remaining components are on the lower level. Radiation entering the interferometer from Port 1 reflects off the input polarizer, P1, down to the concave mirror, M2. Radiation entering from Port 2 reflects off the plane mirror, M1, and the orthogonal component of polarization is transmitted by P1 down to M2. Mirror M2 collimates the radiation through the interferometer, thereby reducing the divergence (of solid angle Ω) so that it does not compromise the maximum attainable resolving power, R, constrained by the Jacquinot criterion ($\Omega R = 2\pi$). The radiation then encounters the polarizing beamsplitter, BS, with its polarization axis oriented to reflect 50% of the incident radiation. The reflected beam is directed to the fixed rooftop mirror, FM, oriented to rotate the plane of polarization by 90° upon reflection such that, upon encountering the beamsplitter a second time, all the radiation is transmitted. The radiation that is initially transmitted by BS reflects off the moving rooftop mirror, MM, again with a 90° rotation in the plane of polarization and again, all of the radiation is reflected upon encountering the beamsplitter a second time. The resulting two beams of orthogonal polarization are directed by the plane mirror M3 to the concave mirror M4 whose focus, after reflection from the plane mirror M5, is at the detector field lens. The final component is the analyser, P2, whose polarization axis is set to combine the two orthogonal beams so that maximum interference occurs.

The infrared interferogram is sampled at equal intervals of optical retardation by the use of an auxiliary laser interferometer. Since the maximum optical retardation is 1.2m, a single-mode stabilised HeNe laser, L1, is required. The laser is directed to the auxiliary interferometer which consists of a beamsplitter, BS′, a fixed corner cube mirror, FM′, and a moving corner cube mirror, MM′, which is mounted on the same translation stage as the moving mirror of the infrared interferometer. Optical interference fringes produced by the recombined beams are detected by the photodiode, D, and resulting signals are electronically amplified and digitized to provide sample pulses for the data acquisition circuitry.

A second HeNe laser, L2, and a novel alignment tool[4], AT, are used to align the interferometer to both the telescope and the detector subsystem. The alignment tool consists of a beamsplitter and a corner cube prism which acts like an an optical *tee* to produce two beams of equal intensity in precisely opposite directions. The center of the beamsplitter lies on the optical axis of the interferometer and the tool can be adjusted by rotation about 3 axes. The alignment tool is mounted on a motorized positioning arm so that it can be accurately and remotely inserted into position to check both the interferometer alignment and the positions of the 2 input ports. This latter feature has been found to be very useful for checking the alignment of the FTS to the telescope and for positioning calibration sources in front of the spectrometer.

2.3 Electronics

The spectrometer is supported by a range of hardware including two IBM PC 486-type microcomputers, an intelligent programmable motor controller and an electronics subsystem responsible for signal conditioning, acquisition and digitization. Each function of the electronics subsystem is associated with a specific module assembled on a high density wire-wrapped board and mounted in a standard subrack assembly. All but the motor controller are located in the observatory control room and communicate with the FTS over a 30m umbilical cable.

2.3.1 Interferometer control

The primary task of this module is to control the motion of the moving mirror and to provide sample pulses for the interferogram. The velocity and acceleration of the moving mirror are controlled by an intelligent programmable controller which uses PID feedback from an integral shaft encoder to control the DC servo motor. At the start of a scan, the motor accelerates to reach a selected constant velocity, after which the moving mirror table passes an optical switch which initiates data acquisition circuitry. The switch provides an absolute index for the co-addition of interferograms and ensures that data are taken only when the mirror is moving at a constant velocity and the laser fringes have stabilised. The laser fringes detected by the photodiode, D, in fig. 1 are filtered, amplified and digitally divided to produce sample pulses whose optical spacing is chosen to satisfy the Nyquist criterion for the wavelengths being measured.

Table 1 Interferometer Characteristics

	Submillimeter configuration	Mid-infrared configuration
Interferometer	Martin-Puplett, double input, single output	
Rapid scan	Maximum scan time 60 seconds	Maximum scan time 5 minutes
Spectral Bands	350 μm = 27.0 – 30.9 cm^{-1} (810 – 927 GHz)	18.4 – 20.4 μm = 490.0 – 545.0 cm^{-1}
	450 μm = 21.4 – 24.2 cm^{-1} (642 – 726 GHz)	
	800 μm = 11.1 – 14.7 cm^{-1} (333 – 441 GHz)	
	850 μm = 11.0 – 12.2 cm^{-1} (330 – 366 GHz)	
	1100 μm = 7.8 – 10.3 cm^{-1} (234 – 309 GHz)	
Resolution	R $\sim$ 7.5 x 10^3 or 40kms^{-1} @ 30 cm^{-1}	R $\sim$ 1.25 x 10^5 or 2.4kms^{-1} @ 500 cm^{-1}
Polarizers	10μm spacing metal grid on 2.5μm Mylar substrate, ϕ = 100mm	2μm spacing metal grid on 4.5μm Polypropylene substrate, ϕ = 75mm
Detector	UKT14, 0.36K bolometer	Si:As photoconductor 4.2K
Beam Width (fwhm)	$\sim$ 6″ - 19″	$\sim$ 1.1′ (for ϕ = 125mm, f/24 solar optics)

2.3.2 Data acquisition

This module is responsible for conditioning and digitizing the analog signal and transmitting the digitized data to the computer. Typically, the detector signal is conditioned by a low noise preamplifier and bandpass filter before entering a programmable-gain amplifier having a high slew rate and fast settling time. In addition to providing gain adjustments to exploit the maximum resolution of the analog-to-digital converter (ADC), this amplifier also allows for gain switching at some appropriate path difference to amplify further the lower intensity region of the interferogram and overcome the dynamic range problem common to all interferometers. The signal then passes to a sample-and-hold circuit which in turn feeds a 16-bit ADC. Digitization is triggered by the sample pulses generated by the control module and the parallel data are directed via DMA to the computer memory.

2.4 Control software

An interrupt-driven *C* program controls the operation of the spectrometer. The computer communicates with the programmable controller through a RS232 interface and with the interferometer electronics through a high speed, 24-bit parallel I/O interface. The program initially checks the interferometer electronics by sending every valid command to each module and reading back the status of the on-board registers. This check takes a few seconds and is able to pinpoint hardware errors in the event of a problem. There are two modes of operation: normal and diagnostic. In the normal mode, the program checks the validity of commands to be sent to the interferometer and aborts transmission if these are found to be invalid (eg. changing the sampling interval during a scan). The diagnostic mode allows the operator complete access to the interferometer control functions and is particularly useful in diagnosing problems or optimising the system. Module level commands set the sampling interval, analog filter, analog gain, velocity and acceleration of the moving mirror and start or stop a scan. From these, a series of higher level commands reset the interferometer, start, truncate or abort a scan sequence, select the resolution by setting the maximum optical retardation and select both the second gain level and the position of activation of this gain change.

In a typical observing sequence, the operator enters a title for the observation, selects the spectral resolution and starts a measurement sequence. The status of the spectrometer is displayed on the control terminal at all times, and includes all error conditions (eg. signal saturation, moving table at its limit, etc). The program also computes and displays other useful information such as the gain setting required to make optimal use of the ADC's dynamic range (typically 90% of full range), or the estimated time to completion of the current scan sequence. A header block containing system parameters is written to computer memory at the start and finish of each scan, on either end of the digitized interferogram signal sequence. At the end of a scan, the data in the computer memory is written to hard disk and the process is repeated for subsequent scans. These header blocks provide a comprehensive log of the observation parameters which is valuable in subsequent data analysis.

2.5 Analysis software

Interferograms are stored on the hard disk of the control computer, but they are also transferred to the analysis computer via a high-speed network that connects the two systems. The data analysis, which consists of phase correction and Fourier transformation of the measured interferograms, is carried out using a library of FORTRAN programs developed for this purpose. The first step is to take the raw interferogram, adjust the data for any gain change which may have occurred during the scan, and then compute the phase error term, $\phi(\sigma)$. This is done by fitting a function to the phase values obtained from the Fourier transform of a short double-sided interferogram, weighted by the amplitude of the corresponding spectrum values. Since the optical elements in the interferometer and detector produce negligible dispersion over the narrow spectral range of interest, in practice this results in a linear phase error. The phase correction function, $\int_{\infty}^{\infty} e^{-i\phi(\sigma)} e^{i2\pi\sigma x} d\sigma$, is computed and convolved with the raw interferogram, $I(x)$, to produce a phase-corrected interferogram. The corrected interferogram can be optimally apodized to reduce the baseline ripple of the instrument function away from the line center of spectral features. Finally the corrected interferogram is zero-infilled and Fourier transformed and the spectral range of interest is written to a disk file. Using a 586/60MHz computer the Fourier transform of an interferogram of 2^{18} real points (each of four bytes), can be computed in a time of 5s. Other programs in the library allow the user to plot and edit interferograms to remove any spikes which may be present, and to co-add, difference, ratio, calibrate and plot spectra.

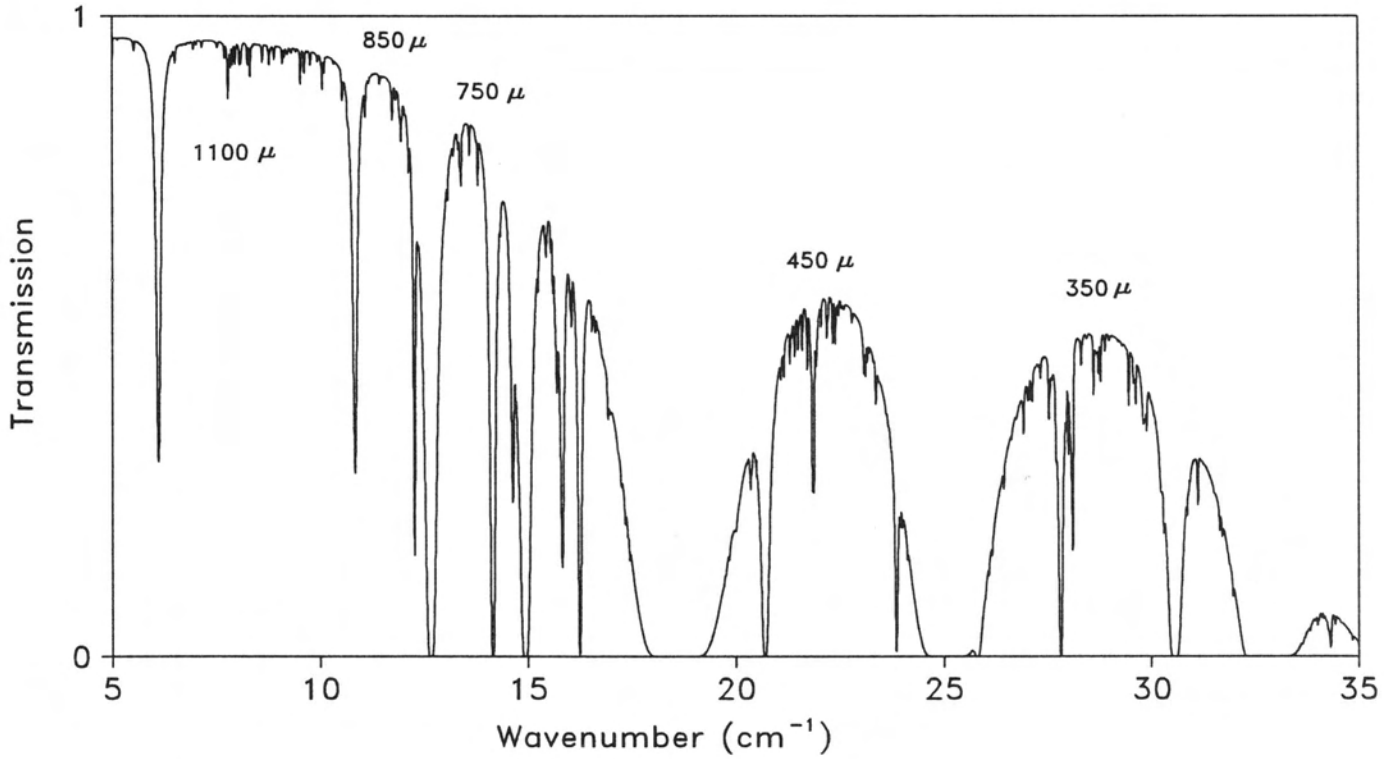

Fig. 2 Zenith transmission above Mauna Kea for 0.5mm precipitable water vapor

3 RESULTS

3.1 Submillimeter observations

The JCMT, situated at an altitude of 4.1 km at the summit of Mauna Kea, Hawaii, features a segmented primary mirror of diameter 15 m, which produces diffraction-limited fields of view of 6–19″. The zenith transmission spectrum of the terrestrial atmosphere above Mauna Kea is shown in fig. 2 for a column water vapor amount of 0.5 mm precipitable, which represents the best of observing conditions. The semitransparent windows at 350 μm and 450 μm are evident, with more pronounced windows at 750 μm, 850 μm and 1.1 mm. The transmission at the shorter wavelengths is critically dependent on the atmospheric water vapor content, which is highly variable in both space and time, and on the poorly characterised H_2O continuum absorption.

The telescope also features a facility photometric detector, UKT14, which is cooled by L^3He to its operating temperature of 0.35 K. The detector cryostat contains a variable aperture and a set of narrowband filters which are matched to the atmospheric windows of fig. 2. Unfortunately, since this detector system was designed for relatively broad-band photometric applications and not for spectroscopy, optical cavities exist within the cryostat which act as parasitic Fabry-Perot interferometers and introduce troublesome channel fringes into the measured spectra. While in principle, channel fringes can be removed by ratioing against spectra of calibration sources, in practice subtle differences in the spectral envelopes make their removal difficult.

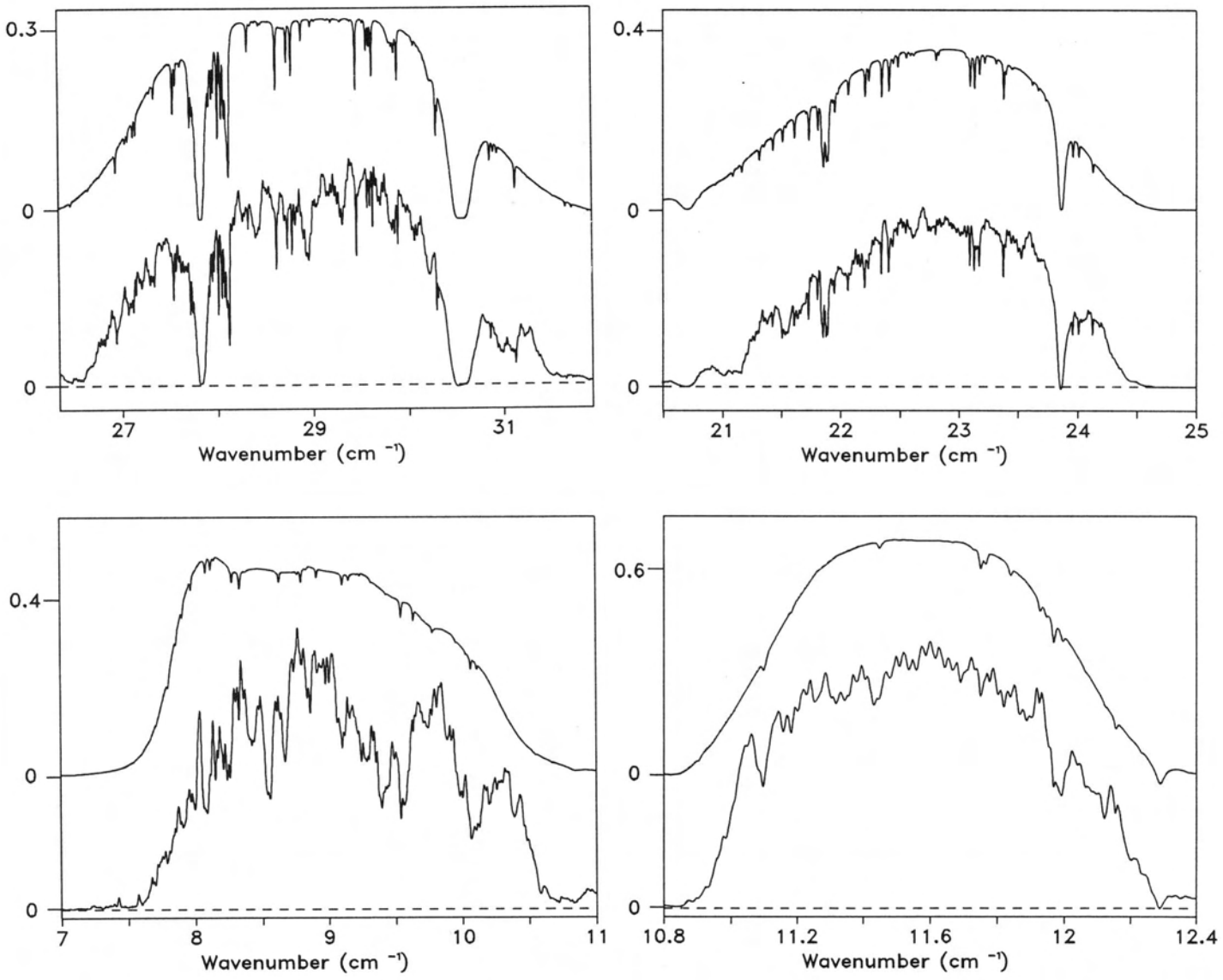

Fig. 3 Synthetic atmospheric transmission spectrum (upper traces) compared with measured solar spectra (lower traces) in the atmospheric windows at 350, 450, 850 and 1100 μm (top left, clockwise)

3.1.1 Submillimeter solar spectroscopy

Since the main source of opacity in the Sun at infrared and submillimeter wavelengths is the free-free transitions of the hydrogen ion, H^-, this spectrum is expected to be largely continuum. The discovery of infrared line emissions from high–n transitions[5,6], the extension of the sequence to far-infrared wavelengths in balloon-borne observations[7] where emission intensities are a few percent of the continuum envelope, and the importance to model calculations of solar limb distributions, led to a series of exploratory observations through the submillimeter atmospheric windows

using the polarizing FTS at the Nasmyth focus of the JCMT[2,8] in a search for Rydberg line features from higher n transitions. This series culminated in May 1993 with a set of solar spectra through 4 submillimeter windows, at 350, 450, 850 and 1100 μm respectively, which cover a range of HI Rydberg transitions from n = 20–19 to 30–29. Representative disk-center solar spectra at each of these wavelengths are shown in fig. 3 along with an equivalent synthetic atmospheric transmission spectrum, adjusted for the transmission of the bandpass filters incorporated in the facility detector, UKT14, used in these measurements. In the 350 and 450 μm windows the syntheses represent excellent fits to the measured spectra. However, in the two longest wavelength bands, at 850 and 1100 μm, the measured spectra become increasingly dominated by channel fringes which arise from optical cavities within the detector subsystem as discussed above.

For the solar observations the second input port of the interferometer viewed an ambient temperature reference source of Eccosorb AN74 (Emerson and Cumming, 604W 182 St, Gardena, CA 90248, USA). Sequential spectra were taken at disk center, at positions near the solar limb and at a sky background reference position displaced in an azimuthal direction by 33′ from the disk center to maintain constant airmass. The major source of noise in these spectra is caused by the variation in the amount of water vapor above the telescope, and therefore in the variation of atmospheric transmission, during the observation and the subsequent non-linear effects of this variation on the transformed spectrum.

Even though the disk center and limb spectra appear virtually identical, subtraction of disk center spectra from those taken at limb shows a significant enhanced limb emission at 29.622 cm^{-1}, the position of the n = 20–19 transition of HI, shown in fig. 4. This represents the first measurement of an HI Rydberg transition at this n level in the solar spectrum. The line intensity at the limb is enhanced by a factor of a few % of the disk center continuum and illustrates the high signal-to-noise of these solar spectra.

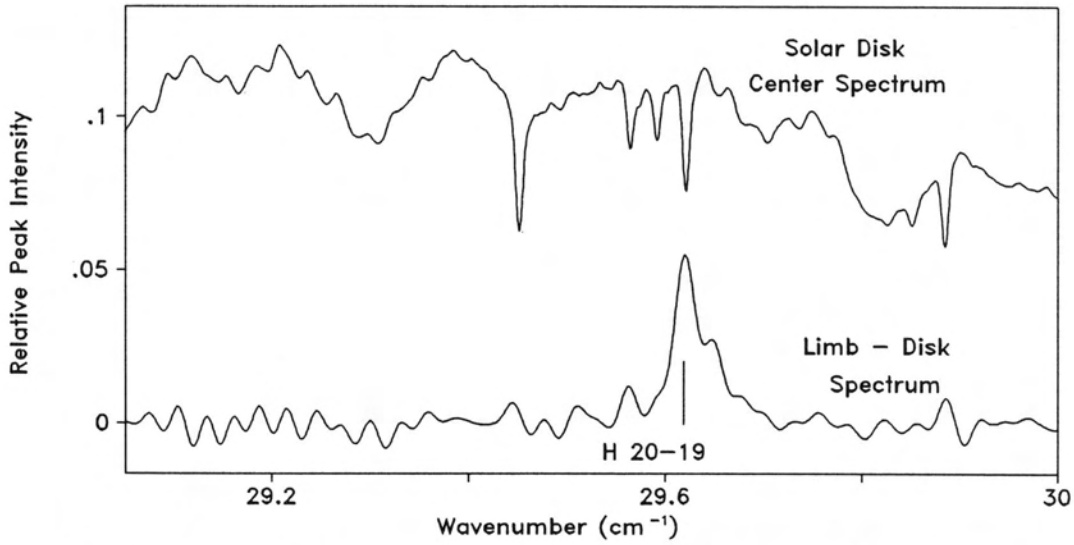

Fig. 4 Detection of solar limb enhanced HI n = 20–19 line emission at 29.622 cm^{-1} (lower trace) compared with disk center spectrum (upper trace)

In addition to adding another measurement to the sequence of HI Rydberg lines which are being used to develop chromospheric models[9], there is further significance to the detection of a line from a transition between such high n levels. Modeling of conditions within the solar chromosphere[10] places limits on the maximum expected principal quantum numbers of HI, and therefore on the effective ionization level of hydrogen (ionization level reduction) and on the broadening of atomic energy levels by interaction of atoms with the plasma (line merging). The effective ionization level is an important parameter in the treatment of the source of the solar continuum radiation and the measurement of this line will place a further constraint on these solar models.

3.1.2 Submillimeter spectroscopy of Uranus and Neptune

The recent and unexpected discovery of CO in the stratosphere of Neptune and its absence in Uranus reinforces the differences between the atmospheres of these planets revealed by Voyager observations. While the bandwidth of the

Rosenqvist *et al.*[11] CO 2–1 (230 GHz) and Marten *et al.*[12] CO 3–2 (345 GHz) heterodyne measurements were insufficient to confirm unambiguously a tropospheric absorption component of CO, these results have important implications for the source of CO in Neptune. If the CO abundance is much smaller in the troposphere than the stratosphere, then the stratospheric CO is probably due to infalling material. If, however, the abundance is constant or decreasing with altitude, as Marten *et al.* suggest, it must originate in the interior of the planet, reaching higher altitudes in Neptune as a result of convection due to its stronger internal heat source. Assuming a uniform vertical distribution for CO, Marten *et al.*[12] present a model which predicts significant pressure-broadened absorption features from the tropospheric component.

This question of the origin of CO in Neptune can only be addressed by spectroscopic measurements over a sufficiently wide enough spectral range. Neither broad-band photometry nor narrow-band heterodyne observations of Neptune are well matched to the width of the strongly pressure-broadened absorption lines (~10 GHz). Since these lines are ideally suited to observation with a Fourier spectrometer, the present polarizing FTS was used in May 1993 to search for CO absorption in the atmosphere of Neptune. Since the Marten *et al.*[12] model predicted the CO 3–2 line to have a full width at half maximum of ~10 GHz or 0.33 cm^{-1}, the resolution of the FTS was set at 0.06 cm^{-1} to allow the line to be resolved adequately. At this resolution the scan time was ~15s. In these measurements the two input ports of the FTS viewed through the telescope and had a separation of 65″ on the sky. The close proximity of Uranus and Neptune (~1.5°) during the observations was key to the success of this technique since it allowed for rapid observations of both planets under essentially the same atmospheric conditions, minimising the influence of atmospheric transmission variations on the measured interferograms, and their non-linear effect on the resulting spectra. During a period of 2 hours, 60 spectra of Uranus and 200 spectra of Neptune were obtained, and these form the basis for the results presented here.

Fig. 5 shows the average of 60 spectra of Uranus (upper trace) and 200 spectra of Neptune (lower trace), presented on the same scale. In the absence of any spectral structure in the source, the result would be the combined transmission profile of the atmosphere plus the instrument. There is a dip in the Neptune spectrum that is not present in the Uranus spectrum, corresponding to an absorption feature at 11.5 cm^{-1} (345 GHz). However, it is also clear that residual channel fringes exist, and that they have different structure for these observations of the two planets.

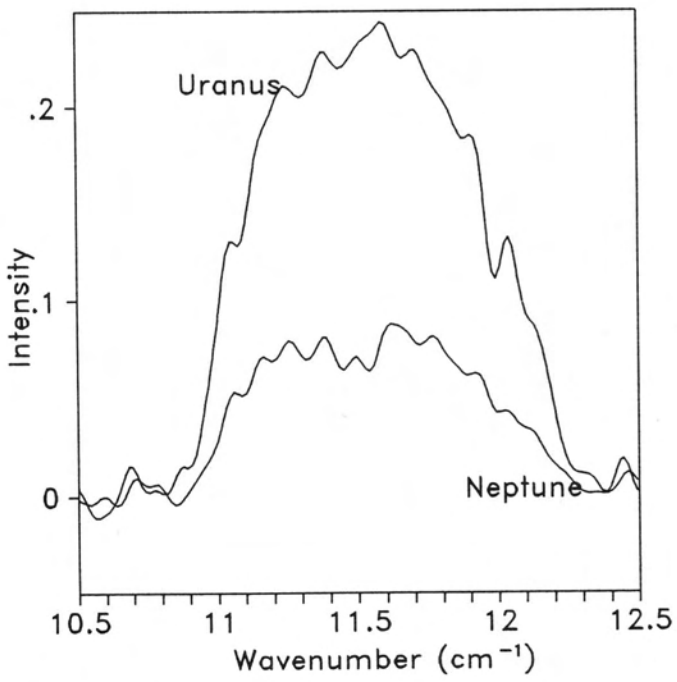

Fig. 5 Averaged spectra of Uranus (upper trace) and Neptune (lower trace) 10.5 – 12.5 cm^{-1}

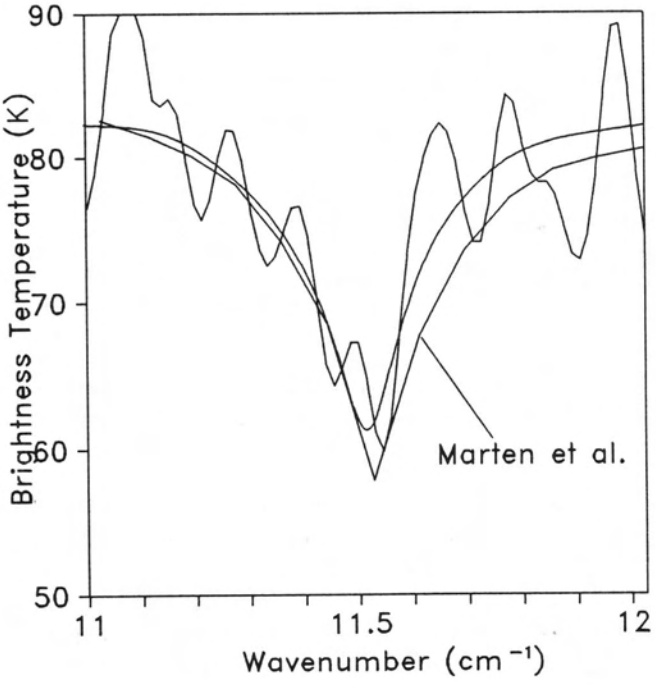

Fig. 6 Neptune brightness temperature showing raw data, spline fit and prediction of Marten *et al.*

Fig. 6 shows the brightness temperature of Neptune, calculated from the ratio of the Neptune/Uranus spectra, and converted to a temperature scale using the model Uranus spectrum of Marten *et al.*[12], taking into account the different solid angles of the two planets. Fig. 6 also shows a filtered spline fit to the raw data and the model Neptune spectrum of Marten *et al.* overlaid without any scaling. Although it is difficult to establish a baseline continuum level for the measured absorption, it is clear that the line is detected in absorption. The spline fit to the measured spectrum is consistent with a somewhat narrower and less intense line than the model prediction. However, given the magnitude of the residual channel fringes, the agreement between theory and observation is encouraging, and illustrates the potential for broad-band intermediate resolution spectroscopy of planetary atmospheres at submillimeter wavelengths. Further FTS observations are planned to determine the CO 3–2 line shape with greater accuracy and to extend the measurement to the CO 2–1 line at 230 GHz. These observations will constrain the CO vertical profile in Neptune.

3.2 Mid-infrared observations

While fabrication methods of early polarizers restricted the useful range of polarizing Fourier spectroscopy to far-infrared wavelengths (>100 cm^{-1}), recent advances in the production of precision, low period (2 μm), large format ($\phi \sim 100$ mm) polarizers offer the exciting potential of extending this range to mid-infrared wavelengths. Free standing wire grids make excellent polarizers for submillimeter and far-infrared applications but extension to shorter wavelengths requires lower period grids which are less tolerant to flatness variations over the area of the polarizer. These more stringent requirements can be met by forming a metal grid on a thin dielectric substrate. Advances in the microelectronics industry, in particular the ability to produce precision, large format, electron beam masks and photolithographic techniques to transfer masks onto substrates, have played a major role in the manufacture of low period and large format polarizers. Since one of our goals was to conduct astronomical observations at wavelengths longward of $\sim 10\mu$m, the presence of strong absorption bands between 400 and 2000 cm^{-1} in Mylar, a common infrared dielectric, precluded its use as substrate. Polypropylene, with its superior transmission characteristics[13], was chosen as the substrate.

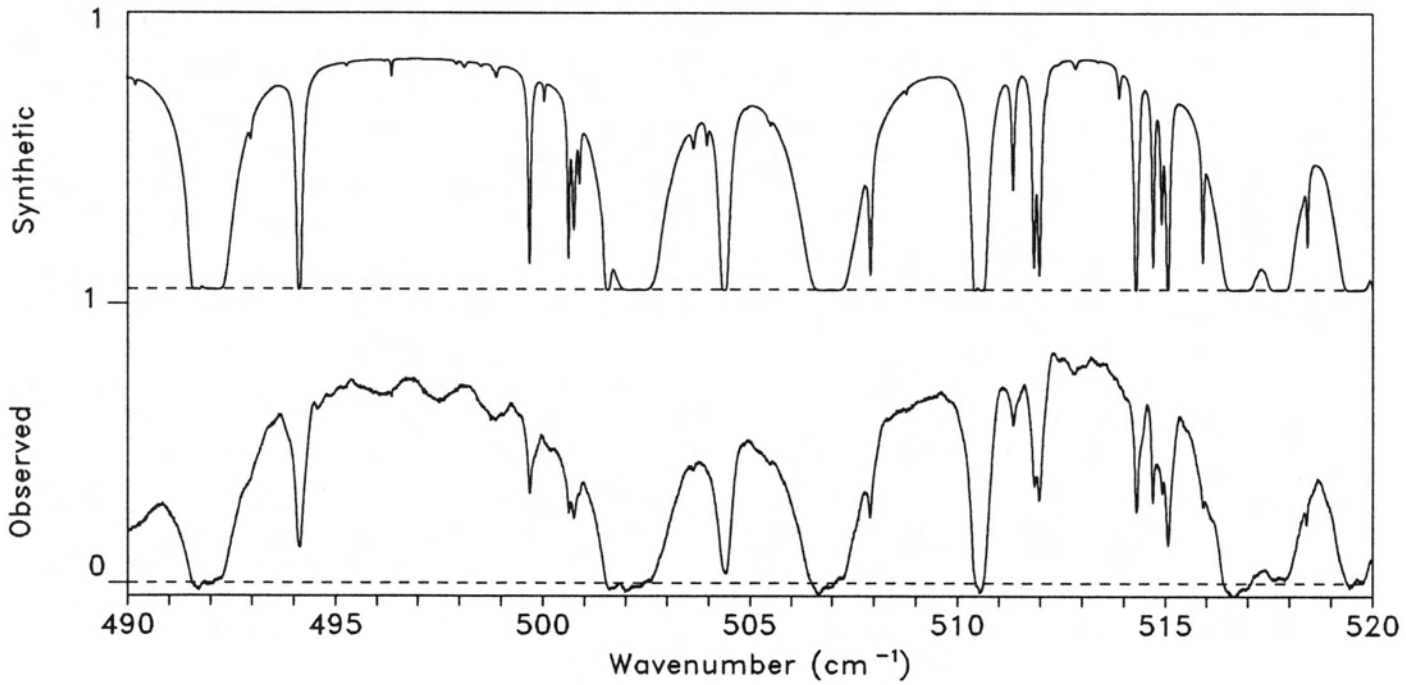

Fig. 7 Synthetic atmospheric transmission spectrum (upper trace) compared with measured solar spectrum (lower trace) in the 20 μm atmospheric window from 490.0 – 520.0 cm^{-1}

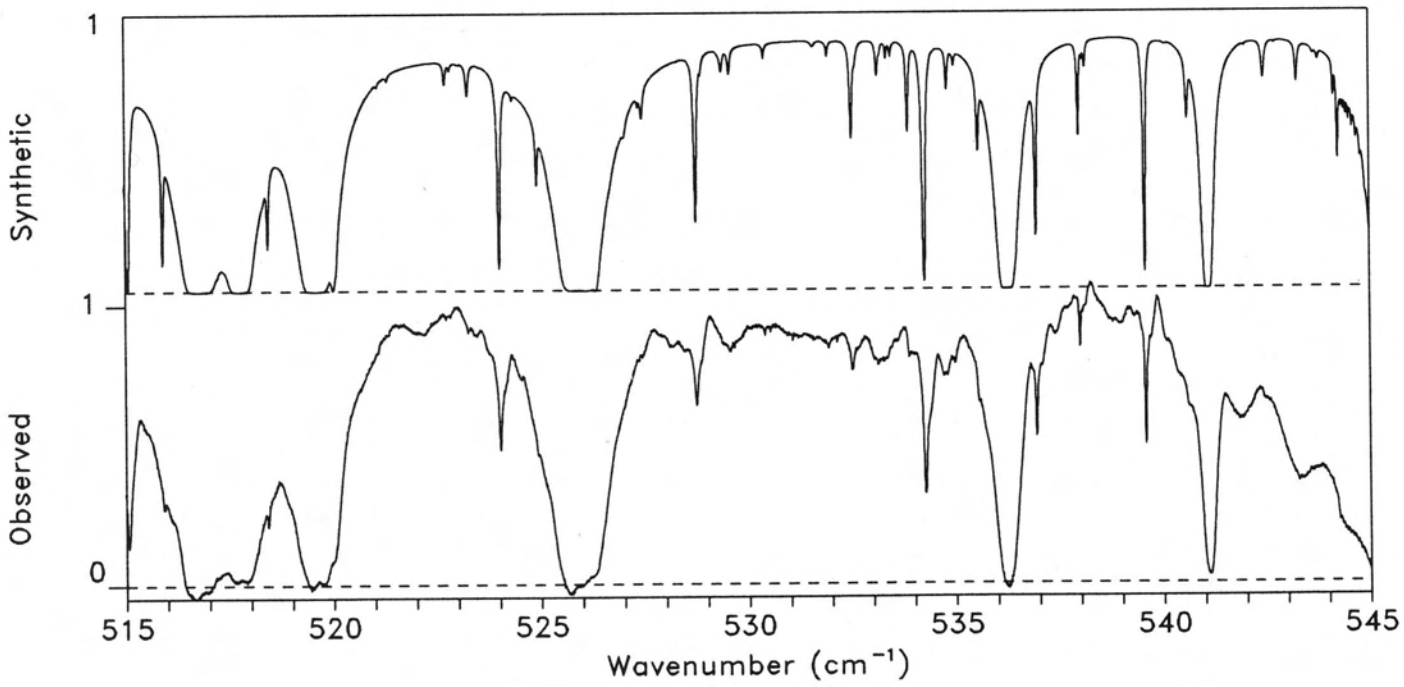

Fig. 8 Synthetic atmospheric transmission spectrum (upper trace) compared with measured solar spectrum (lower trace) in the 20 μm atmospheric window from 515.0 – 545.0 cm^{-1}

3.2.1 Mid-infrared solar spectroscopy

Observations of high–n Rydberg lines in both absorption and emission in the solar infrared spectrum have added a new dimension to the study of the chromosphere[5,6]. The predicted (and, in some cases, observed) sensitivity of these long wavelength lines to atmospheric conditions and magnetic fields via the enhanced Zeeman effect at longer wavelengths, leads to the possibility of magnetic field mapping across regions of the structured chromosphere. In May 1993, a preliminary study was undertaken to determine the feasibility of extending the spectral range of the polarizing FTS to include the 20 μm atmospheric window. A small heliostat mounted above the Coudé room of the NASA Infrared Telescope Facility was used to feed the interferometer. Solar spectra were measured over the range 490–540 cm^{-1}, to a resolution of 0.004cm^{-1}. Figs. 7 and 8 compare the measured solar spectrum with the theoretical atmospheric model. The transmission characteristics of the narrow bandpass filter used in the detector subsystem have not been included in the model. There is seen to be good overall agreement between the two spectra.

Detailed study of the measured solar spectra have led to the detection and preliminary limb distibution of the HI n = 8–7 transition in emission with an intensity of about 3% above the solar continuum envelope at disk center, and of the MgI 8h–7g line in emission near the solar limb[14]. Also evident in these spectra are several sequences of solar OH lines in absorption, the presence of which indicates the existence of cool gas within the hotter chromospheric network, in a manner equivalent to that for the near-infrared vibration-rotation bands of CO[15]. Initial results show that these lines appear at an intensity level of the order of a few percent of the continuum. Further analysis of these and equivalent features will help to understand the nature of this cool solar chromospheric plasma.

To illustrate the performance of the FTS, Fig. 9 shows the detection of the hydrogen 8–7 Rydberg line at 524.61 cm^{-1} on three separate days and at three different resolutions, 0.02 cm^{-1} (lower trace), 0.012 cm^{-1} (middle trace) and 0.004 cm^{-1} (upper trace). The variation in the H_2O abundance over the three days can be readily seen from the nearby $H_2\,{}^{17}O$ isotopic line at 524.94 cm^{-1}, while the hydrogen line intensity remains constant.

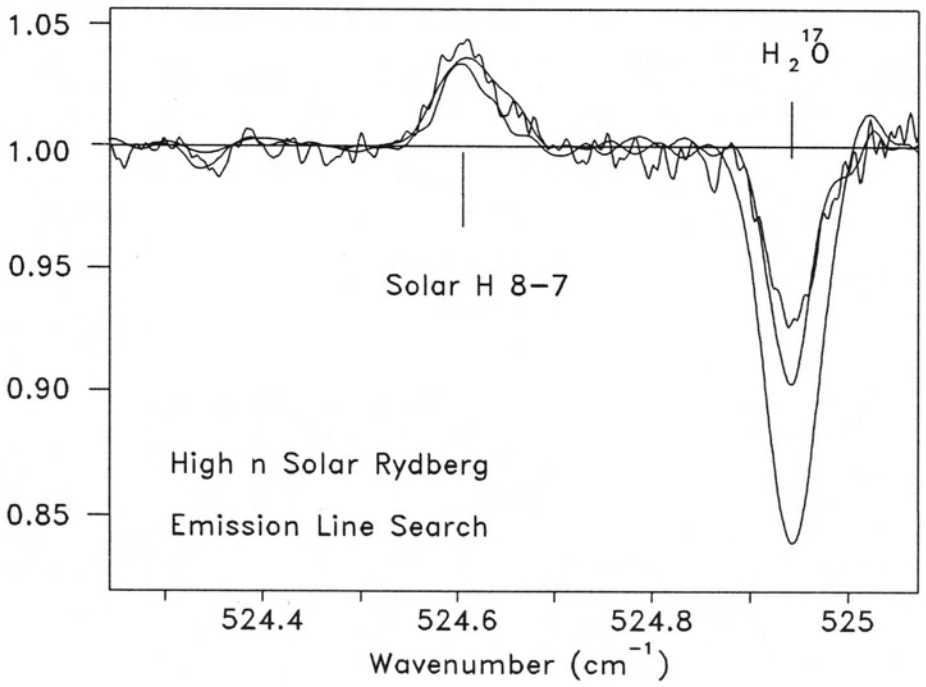

Fig. 9 Detection of the hydrogen n = 8–7 emission line at 524.61 cm^{-1} on three different days. The resolutions are: 0.020 cm^{-1} (lower trace), 0.012 cm^{-1} (middle trace) and 0.004 cm^{-1} (upper trace)

Encouraged by these spectra, the first to be obtained with a polarizing FTS, the future plan is to use the FTS at the Coudé focus of the 3m IRTF telescope, where the higher spatial resolution (~2″) should provide valuable new data on limb brightening at the extreme limb to help in the refinement of atmospheric models, as well as determining whether these emission lines are emitted preferentially from the hot chromospheric network. The ultimate goal of these measurements will be an attempt to map, at the source height of the HI line, the magnetic field distribution across elements of the chromospheric network, a measurement so far not made, even at the modest spatial resolution of this large telescope. Of particular interest in these proposed observations is the possibility of using the two output ports of the FTS to observe simultaneously the adjacent n = 7–6 and 8–7 Rydberg transitions in the 10 and 20 μm windows.

It is interesting to note that as part of an ongoing program of solar spectroscopy, two of us (TAC and DAN) had attempted these measurements in 1986 and again in 1989 using a Michelson interferometer with coated KBr and Mylar beamsplitters, respectively. The weather conditions during the 1989 run were superior (ie. drier) to those encountered during the May 1993 run and yet we were not able to detect the spectral features shown in Fig. 9, even though the same detector and bandpass filter were used in all three sets of observations. Our experience has shown polarizing interferometry to be the most powerful approach to mid-infrared solar astronomical Fourier spectroscopy.

4 CONCLUSIONS

A two-beam polarizing FTS has been developed for broad-band astronomical spectrosopy at submillimeter and mid-infrared wavelengths. The key advantages of the polarizing FTS are a high modulation efficiency over a wide spectral range and an absolute knowledge of the radiation paths to the detector. The ability to reconfigure the spectrometer to observe in any of the submillimeter atmospheric windows in just a few seconds provides high operating efficiency and the flexibility to respond to changing observing conditions. The wide spectral range available with this instrument removes the need for complex cross calibration, since observations are conducted with essentially the same telescope and instrumental parameters at all wavelengths and under the same atmospheric conditions.

The performance of the FTS at submillimeter wavelengths has been determined from a detailed analysis of spectra taken during the May 1993 observing runs. The overall efficiency of the FTS is >90% with signal-to-noise values ranging from 200–1000 per spectral resolution element per scan. We are currently in the process of acquiring a new dual detector system which has been carefully designed to reduce channel fringing. With this system we anticipate that it will be possible to measure line intensities to an accuracy of ~1 K per spectral resolution element of $0.004 cm^{-1}$ in ~15 minutes integration under reasonable observing conditions on the JCMT. The performance of the FTS at mid-infrared wavelengths is still being determined but preliminary results indicate an overall efficiency of ~80% with signal-to-noise values in excess of 100 per spectral resolution element per scan.

5 ACKNOWLEDGEMENTS

The authors would like to thank Mr G. J. Tompkins for the design and construction of the interferometer electronics and for his valuable assistance during observing runs, Mr F. Klassen for his skills in machining critical components of the interferometer, and Dr. P.A.R. Ade for providing the polarizers used in the interferometer. The authors also thank the staff of the James Clerk Maxwell Telescope, which is operated by the Royal Observatory Edinburgh on behalf of the UK Science and Engineering Research Council (SERC), the Netherlands Organisation for Scientific Research (NWO), and the Canadian National Research Council, and the staff of the NASA Infrared Telescope Facility. This research was funded in part by grants from NSERC and NRC, Canada (D.A.N., T.A.C. and G.R.D.).

6 REFERENCES

1 Naylor, D.A. & Clark, T.A., "A Mid-infrared astronomical Fourier transform spectrometer", *Instrumentation in astronomy VI* (Ed. Crawford, D.L.) SPIE **627**, pp.482–490, 1986.
2 Naylor, D.A., Clark, T.A., Schultz, A.A. & Davis, G.R., "Atmospheric transmission at submillimetre wavelengths from Mauna Kea", *Mon. Not. R. Astr. Soc.* **251**, pp. 199–202, 1991.
3 Martin, D.H. & Puplett, E.F., "Polarised interferometric spectroscopy for the millimetre and submillimetre spectrum", *Infrared Physics*, **10**, pp. 105–109, 1970.
4 Naylor, D.A., "A versatile optical alignment tool", *Engineering & Laboratory Notes* (In press).
5 Murcray, F.J., Goldman, A., Murcray, F.H., Bradford, C.M., Murcray, D.G., Coffey, M.T. & Mankin, W.G., "Observation of new emission lines in the infrared solar spectrum near 12.33, 12.22 and 7.38 μm", *Ap. J.*, **247**, pp. L97–L99, 1981.
6 Brault, J. & Noyes, R.W., "Solar emission lines near 12μm", *Ap. J.*, **269**, pp. L61–L66, 1983.
7 Boreiko, R.T. & Clark, T.A., "Far IR solar emission lines from high n states of hydrogen", *Astron. Ap.*, **157**, pp. 353–356, 1986.
8 Naylor, D.A., Clark, T.A., Davis, G.R., Duncan, W.D. & Tompkins, G.J., "Broad-band spectroscopy with the James Clerk Maxwell telescope using a polarizing Fourier transform spectrometer", *MNRAS* **260**, pp. 875–882, 1993.
9 Carlsson, M. & Rutten, R.J., "Computation of infrared hydrogen lines", *IAU symposium 154: Infrared Solar Physics*, (Eds. Rabin, D.M., Jefferies, J.T. & Lindsey, C), pp. 341–346, 1994.
10 Kunc, J.A. & Soon, W.H., "Maximum principal quantum numbers of the atomic hydrogen in the solar chromosphere and photosphere", *Ap. J.*, **296**, pp. 364–368, 1992.
11 Rosenquist, J., Lellouch, E., Romani, P.N., Paubert, G. & Encrenaz, T., "Millimeter-wave observations of Saturn, Uranus and Neptune: CO and HCN on Neptune", *Ap. J.* **392**, pp. L99–L102, 1992.
12 Marten, A, Gautier, D, Owen, T, Sanders, D.B., Matthews, H.E., Atreya, S.K., Tilanus, R.P.J. & Deane., J.R., "First observations of CO and HCN on Neptune and Uranus at millimeter wavelengths and their implications for atmospheric chemistry", *Ap. J.* **406**, pp. 285–297, 1993.
13 Labrie, D., Booth, I.J., Thewalt, M.L.W. & Clayman, B.P., "Use of polypropylene film for cryogenic windows", *Appl. Opt.*, **25**, pp. 171–172, 1986
14 Clark, T.A. & Naylor, D.A. (In preparation)
15 Ayres, T.R., "Thermal bifurcation of the outer photosphere", *IAU symposium 138: Solar Photosphere: Structure, Convection and Magnetic Fields*, (Ed. Stenflo, J.O.), pp. 23–27, 1990.